Azizzadeh *et al.*
Environmental Sciences Europe (2022) 34:49
https://doi.org/10.1186/s12302-022-00627-x

Environmental Sciences Europe

RESEARCH Open Access

Ternary metal-organic framework/multi-walled carbon nanotube/iron oxide nanocomposite for removal of butachlor pesticide

Ali Azizzadeh[1], Ali Akbar Amooey[1*] and Shahram Ghasemi[2]

Abstract

Background: Butachlor (BUT) as an organochlorine pesticide (OCP) that prevents weeds from growing has been used in the agriculture field. It remains in the environment for a long time and causes mutagenicity and cancer.

Results: In the current study, magnetic multi-walled carbon nanotube with zeolitic imidazolate frameworks-67 (Fe_3O_4–MWCNT–ZIF67) was used as adsorbent to remove BUT from the aqueous solution. The characteristics and the chemical composition of the adsorbent were evaluated using FE-SEM, TEM, MAP, EDX, FTIR, BET, TGA and VSM. The response surface methodology (RSM) as a method for the design of experiment was applied to optimize variables such as the initial concentration of BUT, adsorbent dosage, contact time and temperature in the batch experiment by central composite design (CCD). The optimum adsorption condition predicted by RSM was pH = 4.5, initial concentration = 5.75 ppm, dosage = 0.07 g and contact time = 95 min. The results showed that maximum removal efficiency for the butachlor is 86%.

Conclusions: Different adsorption isotherms were evaluated using adsorption equilibrium data and results showed that Temkin model has the best compatibility with the experimental data. In addition, the adsorption kinetics data were closer with pseudo-second-order model. Thermodynamic study showed that the adsorption process was spontaneous, endothermic and physical. This composite can be effectively used for the remediation/clean-up of groundwater and agricultural run-off water which are contaminated with harmful pesticides.

Keywords: Adsorption, Butachlor, Magnetic nanocomposite, Metal–organic framework, Response surface methodology

*Correspondence: aliakbar_amooey@yahoo.com; aamooey@umz.ac.ir

[1] Department of Chemical Engineering, Technology and Engineering of Faculty, University of Mazandaran, Babolsar, Iran
Full list of author information is available at the end of the article

Graphical Abstract

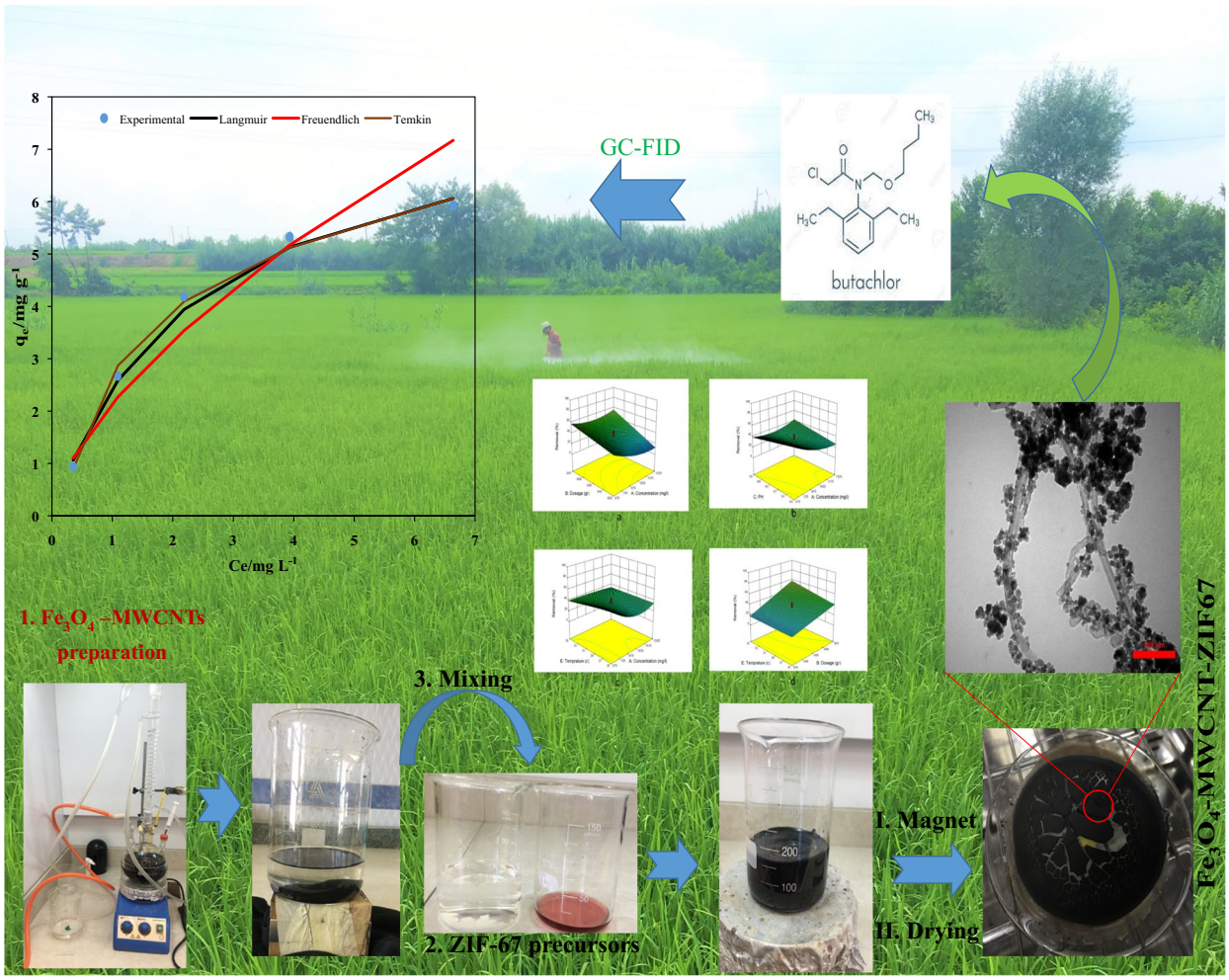

Introduction

According to some studies, the most important environmental pollutants are pesticides and fertilizers [1, 2]. Excessive use of pesticides in the agricultural industry causes environmental pollution, especially in water resources. Organochlorine (OC) toxins can stay in the environment for long time. Even low concentration of OCs is harmful to human health and they can accumulate in tissues due to their low rate of chemical and biological degradation and hydrophobicity. With increasing their concentrations, they enter to the food cycle and affect the nervous system and cause carcinogenicity. According to the European Union, the amount of pesticides in drinking water should not exceed 0.1 μg L^{-1} [3].

One of the organochlorine pesticides (OCP) is *N*-(butoxymethyl) 2-chloro 2',6'-diethyl acetanilide known as butachlor (BUT). It is widely used in African and Southeast Asian countries such as China, India and Iran. BUT is used to prevent weeds in rice, wheat, barley, sugarcane, cotton and corn fields [4].

Numerous adsorbents have been used to remove pesticides, such as two-dimensional carbon materials including graphene oxide [5], carbon nitride [6], silica particles [7], magnetic materials [8], and organic porous polymers [9]. Carbon nanotubes (CNT) are nanomaterial with one-dimensional and multidimensional tubular structure [10]. Due to their small radial dimension, special surface area, outstanding

mechanical properties, electrical and thermal conductivity, they have excellent effect in adsorbing inorganic and organic pollutants from solutions, such as heavy metal ions [11], antibiotics [12], dyes [13], and other organic materials [14].

Multi-walled carbon nanotubes (MWCNTs) are composed of graphene sheets with high specific surface area, hollow porous structure, and excellent stability, which make them suitable as adsorbents [15]. Functionalized CNTs have strong interaction with organic molecules through non-covalent forces such as hydrogen bonding, π–π bonding, electrostatic force, and hydrophobic interaction, which leads to increased special benefits in the removal of organic pollutants. However, MWCNTs are 1D nanomaterials and it is difficult to separate them from the aqueous solutions, which limits their application. For easy separation, they can be combined with iron oxide (Fe_3O_4) to form a magnetic composite [10].

New adsorbents such as metal–organic frameworks (MOF) have recently received much attention due to high surface area and porosity. Metal centers coordinated with oxygen or nitrogen atoms are connected by linkers to aromatic rings. The main characteristics of MOFs are strong crystalline frames with permanent porosity, crystalline properties, super-adjustable porosity, variable structure, large surface area and pore volume, uniform pore size, and special sites for selective adsorption [16]. Due to their high removal ability, they are ideal options for various applications such as removal of pollutants [17], fuel storage (methane and hydrogen) [18], carbon dioxide adsorption [19], sensor, photocatalytic degradation [20], catalytic purpose [21], separation [22], membrane [23] and heterogeneous decomposition [24].

Zeolite imidazolate frameworks (ZIF) are one example of MOFs, which has well-formed porous and three-dimensional structure. Due to their high specific surface area, high adsorption capacity, often high chemical and physical stability, they have been considered in many different fields such as: gas storage [25], separation [26], catalyst [27], contaminant removal [28], chemical sensors [29] and drug delivery [30]. The properties, type and structure of ZIF depend on different combinations of imidazole binders and metal ions. Many synthetic ZIF structures have been reported. It is possible to synthesize them using different transition metals (such as zinc and cobalt), imidazole binders (such as: 2-methylimidazole and benzimidazole) and solvents such as: water, dimethylformamide, diethylformamide, ethanol and methanol [31, 32]. ZIF-67 is a conventional MOF made from binding the cobalt ion and 2-methylimidazole ligand. Due to its attractive structure, large surface area, distinct morphology, permanent nanoscale porosity and excellent chemical stability, it is widely used in various fields such as separation [33], adsorption [34], inhomogeneous decomposition [35], oxygen evolution [36] and electrochemical reaction [37].

There is limited research on the removal of BUT by adsorption method [38]. With this aim, a composite of magnetic carbon nanotubes with ZIF-67 was fabricated and used as an adsorbent for BUT removal. In addition, the effect of parameters such as initial herbicide concentration, adsorbent dosage, pH, contact time and temperature were investigated using experimental design method.

Materials and methods

Chemicals

$Co(NO_3)_2$ $0.6H_2O$, 2-methylimidazole (2MIM), $FeCl_2$ and $FeCl_3$, ammonium hydroxide solution (25%), HNO_3 (65%) and sulfuric acid (98%) were all provided by Merck Company. MWCNT (diameter of 30–50 nm) was purchased from Sigma-Aldrich. BUT toxin with 98% purity was provided by Golsam Company (Golestan province, Iran).

Adsorbent synthesis

ZIF-67

The ZIF-67 was synthesized according to the literature with little modification. First, 0.45 g of 2MIM and 0.45 g of $Co(NO_3)_2.6H_2O$ were dissolved separately in 20 mL and 3 mL water. $Co(NO_3)_2$ solution was then added to the 2MIM solution and the mixture was stirred at room temperature for 6 h. The resulting purple precipitate (ZIF-67) was collected by centrifugation, washed with distilled water and then with ethanol for several times, and finally dried in oven at 60 °C for 24 h [39].

Functionalization of MWCNT

To oxidize and functionalize MWCNTs, 2 mL of nitric acid and 1.8 mL of H_2SO_4 were added separately to two 100-mL volumetric balloons. Then, 25 mL of HNO_3 and 75 mL of H_2SO_4 were mixed with volume ratio of 1:3 and 0.6 g of MWCNTs was added to the mixture. It was irradiated in an ultrasonic batch for 2 h at 40 °C and then rinsed several times with distilled water and centrifuged. The precipitate was dried at 60 °C in an oven for 60 h.

Preparation of Fe_3O_4–MWCNT

At this stage, the synthesis of Fe_3O_4–MWCNT was performed by co-precipitation method. First, 0.6 g of MWCNT was added to 720 mL of distilled water and irradiated by ultrasonic for 1 h to obtain a homogeneous and dispersed mixture in water and then transferred to a three-neck round-bottom flask. The temperature of the hot water bath was set at 80 °C. 2.4 g of $FeCl_2$ and 5.4 g of $FeCl_3$ with 50 mL of distilled water were added to the balloon and allowed to mix for 1 h under N_2 atmosphere,

and then 17 mL of ammonium solution was added drop-by-drop into flask for 20 min. The mixture was stirred for another 1 h to allow the reaction of any unreacted materials. The product was washed using water and ethanol with a volume ratio of 1:1. The washing step was continued until the pH reaches neutral values. A strong magnet was used to separate the sediment. The precipitate was then dried in a vacuum oven at 60 °C for 24 h.

Fe_3O_4–MWCNT–ZIF67

2.4 g of Fe_3O_4–MWCNT was mixed with 60 mL of distilled water and subjected to ultrasonic irradiation for 30 min. 1.35 g of $Co(NO_3)_2.6H_2O$ and 1.35 g of 2-MIM were mixed separately in 9 and 60 mL of water, respectively. The dissolved cobalt nitrate solution was added to the Fe_3O_4–MWCNT in a beaker and placed on a magnetic stirrer for 30 min. Then 2-MIM solution was added to the mixture and stirred for another 6 h. Water and ethanol with a volume ratio of 1:1 were used to wash the precipitate and a strong magnet was used to collect the particles from the mixture. The washing step was performed several times to reach the pH of mixture to neutral range. The product was then transferred to a vacuum oven for drying at 60 °C for 24 h.

Adsorbent characterization

To determine the morphology and characteristics of adsorbent, field emission scanning electron microscope (FE-SEM) (TESCAN, MIRA III) and transmission electron microscopy (TEM, Philips, accelerating voltage of 100 kV) were used. X-ray diffraction (XRD) (PHILIPS, PW1730) was performed to investigate the crystal structure of samples. Fourier transform infrared spectroscopy (FTIR) was conducted to identify the functional groups and molecular structure (Thermo, AVATAR). For chemical identification of materials, energy dispersive X-ray spectroscopy (EDS) and mapping analysis were used to provide the frequency distribution of available elements (TESCAN, MIRA III). To investigate the porosity and surface area of Fe_3O_4–MWCNT–ZIF67 nanocomposite, N_2-adsorption/desorption isotherm was recorded using BELSORP MINI II. To determine the thermal stability of the adsorbent, TGA analysis (by TA, Q600) was applied in the temperature range of 25–800 °C under argon gas with a heating rate of 10 °C min^{-1}. A vibrating-sample magnetometer (Meghnatis Daghigh Kavir Co. Kashan, Iran) was used to investigate the magnetic properties of the adsorbent.

Removal of BUT herbicide

Adsorption experiments

In order to investigate the batch adsorption process, the effect of various parameters such as adsorbent dosage (0.01–0.09 g), pH (3–9), initial solution concentration (2–17 ppm), contact time (5–125 min) and temperature (20–40 °C) were evaluated using a design of experiments (DOE).

Various experiments were defined and performed to evaluate the efficiency of adsorbent and the effect of different parameters on the rate of toxin adsorption. To prepare the stock solution of BUT (17 ppm), it was dissolved in acetone and all the required concentrations were diluted using the same stock solution. 50 mL of solution containing pesticide in certain concentrations was added to an Erlenmeyer with a volume of 100 mL, and after adjusting the pH of the solution, a certain mass of adsorbent was added to the solution. The Erlenmeyer is then transferred to an incubator shaker so that the solution and the adsorbent are in contact under the defined operating conditions. Then, after a certain period of time, some of the solution was separated using a strong magnet in order to separate the adsorbent particles from the solution. Gas chromatography coupled with flame-ionization detector (GC-FID, Agilent 6850) was used for determination of BUT residues and stock solution concentration. The capillary column HP-5 (30 m × 0.25 mm × 0.25 μm) was used for separation. Nitrogen was used as the carrier gas at a flow rate of 1 mL min^{-1}. The following temperature program was employed: initial temperature of 180 °C held for 3 min; increased at 30 °C min^{-1} to 240 °C, total runtime of 8 min. The injector and detector temperatures were 260 °C. To extract the BUT from aqueous solution, ethyl acetate was used.

The following equation was used to calculate the removal percentage of BUT pesticide:

$$\text{BUT removal\%} = \left(\frac{C_0 - C_t}{C_0}\right) * 100, \tag{1}$$

where C_0 and C_t are initial concentration and concentration of the BTU in solution at time t.

Design of experiments

Response surface methodology (RSM) is a set of mathematical and statistical methods that are used in DOE, model development, factor evaluation and condition optimization. In order to investigate the main factors in the process of removing BUT toxin, the interactions among them, and also minimize the number of experiments, the central composite design (CCD) method, which is one of the methods of the RSM family, was utilized. In this work, five variable factors including initial concentration of BUT, pH, adsorbent dosage, contact time and temperature were considered. The lower, middle, and upper limit ranges of CCD are tabulated in Table 1. Analysis of variance (ANOVA) was performed

Table 1 Range and levels of laboratory independent variables

Variable	Axial bottom (−α)	Low factorial (−1)	Central point (0)	High factorial (+1)	High axial (α)
Concentration (ppm)	2	5.75	9.5	13.25	17
Dosage (g)	0.01	0.03	0.05	0.07	0.09
pH	3	4.5	6	7.5	9
Time (min)	5	35	65	95	125
Temp (°C)	20	25	30	35	40

by determining the correlation coefficient (R^2). The statistical values of the coefficients of the approach and model variables were measured based on probability. The experimental design was done with Design Expert software version 10. The design of the semi-partial rule experiment was performed. The total number of experiments is 36 (Table 2). The purpose of response surface optimization is to determine the optimal maximum or minimum location in the design space that the response is stable. Response surface optimization is obtained with Design Expert software version 10 and based on the model equation. After determining the optimal conditions by the model, the last step was done at the optimum point to confirm the credibility of the model.

Adsorption isotherm

To study the adsorption process, Langmuir, Freundlich and Temkin isotherms were investigated to describe the adsorption isotherms of Fe_3O_4–MWCNT–ZIF67 for removal of BUT pesticide.

Langmuir model assumes monolayer coverage on adsorbent [40]:

$$q_e = \frac{q_{\max} K_L C_e}{1 + K_L C_e}, \tag{2}$$

where q_e and $q_{\max}$(mg g^{-1}) indicates equilibrium adsorption capacity and maximum adsorbent capacity; K_L (L mg^{-1}) equilibrium constant and C_e (mg L^{-1}) is equilibrium concentration.

Freundlich model is an empirical model allowing for multilayer adsorption on adsorbent [41]:

$$q_e = K_F C_e^{1/n}, \tag{3}$$

where K_f and n are the Freundlich constants. K_f is roughly an indicator of the adsorption capacity (L g^{-1}) and 1/n is an empirical parameter relating the adsorption intensity. Temkin model interaction between adsorbent and adsorbed considers [42]:

$$q_e = \left(\frac{RT}{B_T}\right) Ln(K_T C_e), \tag{4}$$

where K_T and B_T Temkin constant; R general gas constant; (8.314 J mol^{-1} K^{-1});and T is the absolute temperature (K).

Adsorption kinetics

Kinetic study provides information about rate of process throughout of adsorption pathway. There are several adsorption kinetic models for analyzing of experimental data. In this study, the pseudo-first-order kinetic model and pseudo-second-order kinetic model were investigated.

The pseudo-first-order kinetic model was generally expressed as the following equation [43]:

$$\log(q_e - q_t) = \log q_e - \frac{K_1}{2 \cdot 303} t, \tag{5}$$

where K_1 is the constant speed (min^{-1}); parameters q_t and q_e, respectively, the adsorption capacity is at time t and equilibrium time (mg g^{-1}). The pseudo-second-order kinetic model was expressed as following [44]:

$$\frac{t}{q_t} = \frac{1}{h} + \frac{t}{q_e}, \tag{6}$$

where $h = K_2 q_e^2$ initial species uptake rate; the parameter K_2 is the quadratic velocity constant of the relation, $h = K_2 q_e^2$ are obtained.

Another kinetic model is the Elovich model which is represented as follows [45]:

$$q_t = \frac{1}{\beta} \ln(\alpha\beta) + \frac{1}{\beta} \ln(t) \tag{7}$$

The parameter α is the initial adsorption rate of Elovich equation (mg g^{-1} min^{-1}) and β is the desorption constant (g mg^{-1}).

A model on the basis of intra-particle diffusion theory was proposed by Weber and Morris was investigated.

Table 2 Total number of experiments

Std.	Block	Run	*A*: concentration (ppm)	*B*: dosage (gr)	*C*:pH	*D*: time (min)	*E*: tempe (°C)	Response removal %
14	Day1	1	13.25	0.03	7.5	95	25	37.6112
9	Day1	2	5.75	0.03	4.5	95	25	63.4589
1	Day1	3	5.75	0.03	4.5	35	35	25.5359
20	Day1	4	9.5	0.05	6	65	30	42.7421
18	Day1	5	9.5	0.05	6	65	30	37.0163
17	Day1	6	9.55341	0.05	6	65	30	35.694
5	Day1	7	5.75	0.03	7.5	35	25	44.5341
21	Day1	8	9.5	0.05	6	65	30	39.912
6	Day1	9	13.25	0.03	7.5	35	35	21.7093
10	Day1	10	13.25	0.03	4.5	95	35	6.9871
24	Day1	11	9.5	0.05	6	65	30	38.8849
7	Day1	12	5.75	0.07	7.5	35	35	31.2209
13	Day1	11	5.75	0.03	7.5	95	35	27.5952
2	Day1	14	13.25	0.03	4.5	35	25	8.4832
19	Day1	15	9.5	0.05	6	65	30	40.0994
8	Day1	16	13.25	0.07	7.5	35	25	60.1487
15	Day1	17	5.75	0.07	7.5	95	25	67.5347
16	Day1	18	13.25	0.07	7.5	95	35	79.6741
22	Day1	19	9.5	0.05	6	65	30	41.9663
11	Day1	20	5.75	0.07	4.5	95	35	85.7869
3	Day1	21	5.75	0.07	4.5	35	25	61.5044
4	Day1	22	13.25	0.07	4.5	35	35	53.2293
12	Day1	23	13.25	0.07	4.5	95	25	59.8452
23	Day1	24	9.5	0.05	6	65	30	40.4256
32	Day2	25	9.5	0.05	6	125	30	21.8978
25	Day2	26	2	0.05	6	65	30	78.1712
27	Day2	27	9.5	0.01	6	65	30	1.9092
31	Day2	28	9.5	0.05	6	5	30	24.013
34	Day2	29	9.5	0.05	6	65	40	34.6366
26	Day2	30	17	0.05	6	65	30	39.2351
35	Day2	31	9.5	0.05	6	65	30	26.9979
29	Day2	32	9.5	0.05	3	65	30	36.1749
33	Day2	33	9.5	0.05	6	65	20	17.0762
30	Day2	34	9.5	0.05	9	65	30	31.3592
28	Day2	35	9.5	0.09	6	65	30	58.3809
36	Day2	36	9.5	0.05	6	65	30	24.6729

According to this model, adsorption capacity is proportional to the square root of time [46]:

$$q_t = K\, t^{0.5} + C \tag{8}$$

The parameter K is intra-particle diffusion rate constant and C is boundary layer thickness constant.

Thermodynamic studies

The effect of temperature on removal percentage was investigated in the range of 20–40 °C. Important thermodynamic parameters such as Gibbs free energy change (ΔG°), standard enthalpy (ΔH°) and standard entropy (ΔS°) were calculated as follows [47]:

$$\Delta G^0 = \Delta H^0 - T\Delta S^0 \tag{9}$$

$$ln\mathrm{Kd} = \frac{\Delta S^0}{R} - \frac{\Delta H^0}{RT}, \tag{10}$$

where R is the universal gas constant (8.314 J mol^{-1} K^{-1}), T is the absolute temperature (K) and K_d is the thermodynamic equilibrium constant, determined from $\frac{qe}{Ce}$.

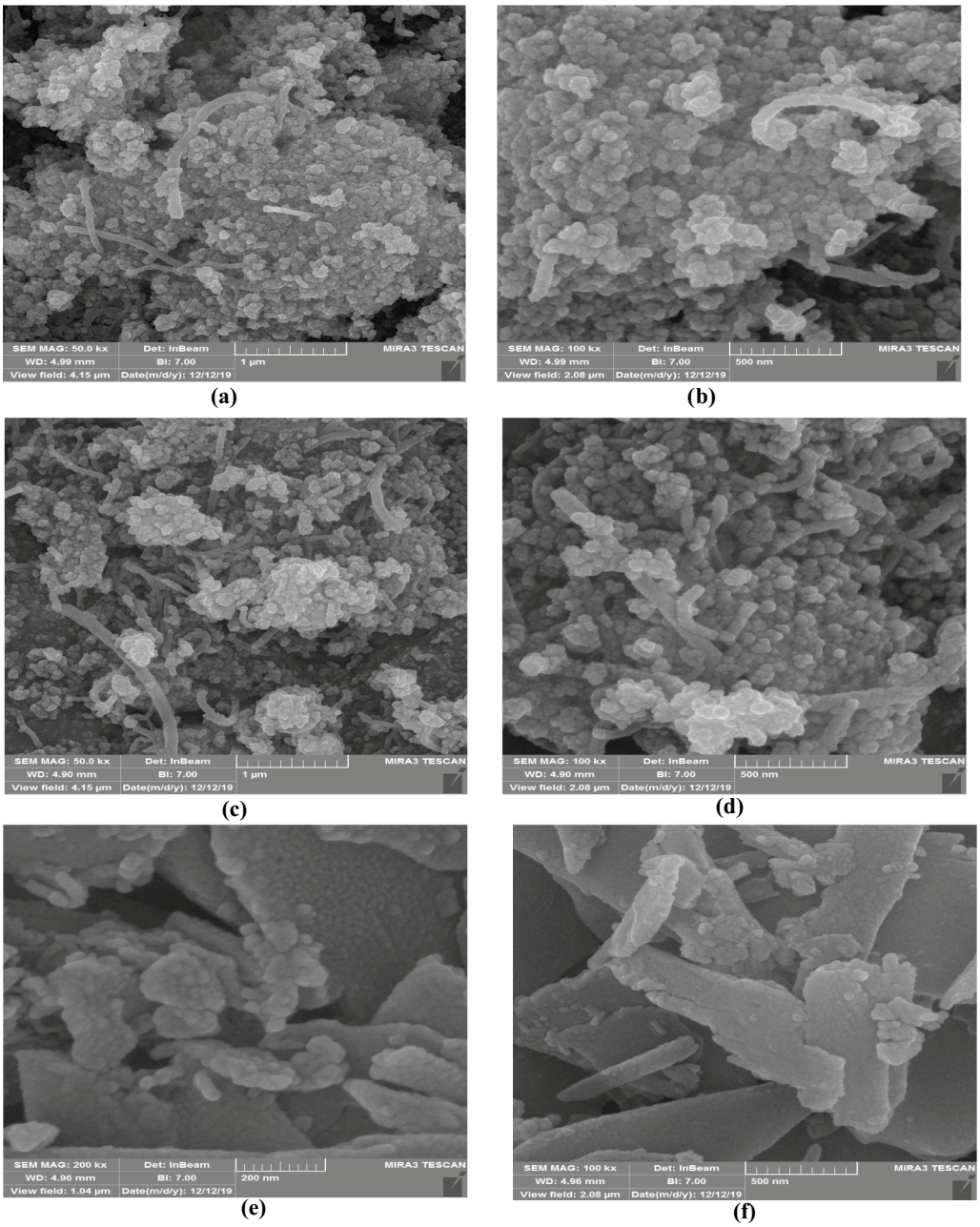

Fig. 1 FE-SEM images of **a**, **b** Fe_3O_4–MWCNT, **c**, **d** Fe_3O_4–MWCNT–ZIF67 and **e**, **f** ZIF67

Results and discussion

Characterizations of Fe_3O_4–MWCNT-OH/ZIF67

Figure 1a, b shows the FE-SEM images of Fe_3O_4–MWCNT at two different magnifications. Spherical Fe_3O_4 nanoparticles are formed on the surface of MWCNT and aggregated to each other. Figure 1c, d shows the morphology of Fe_3O_4–MWCNT–ZIF67, in which the MWCNTs and other nanoparticles with sizes lower than 100 nm can be observed in the image. It seems that with addition of ZIF-67 to the structure of sample, the aggregation of sample is somewhat decreased. In addition, Fig. 1e, f shows the structure of ZIF-67 which are composed of some spherically interconnected nanoparticles in the form of plates.

TEM was used to obtain more information about the structure of Fe_3O_4–MWCNT–ZIF67 at different magnifications (Fig. 2). MWCNTs can be observed in the images and some nanoparticles are attached to them. The dark

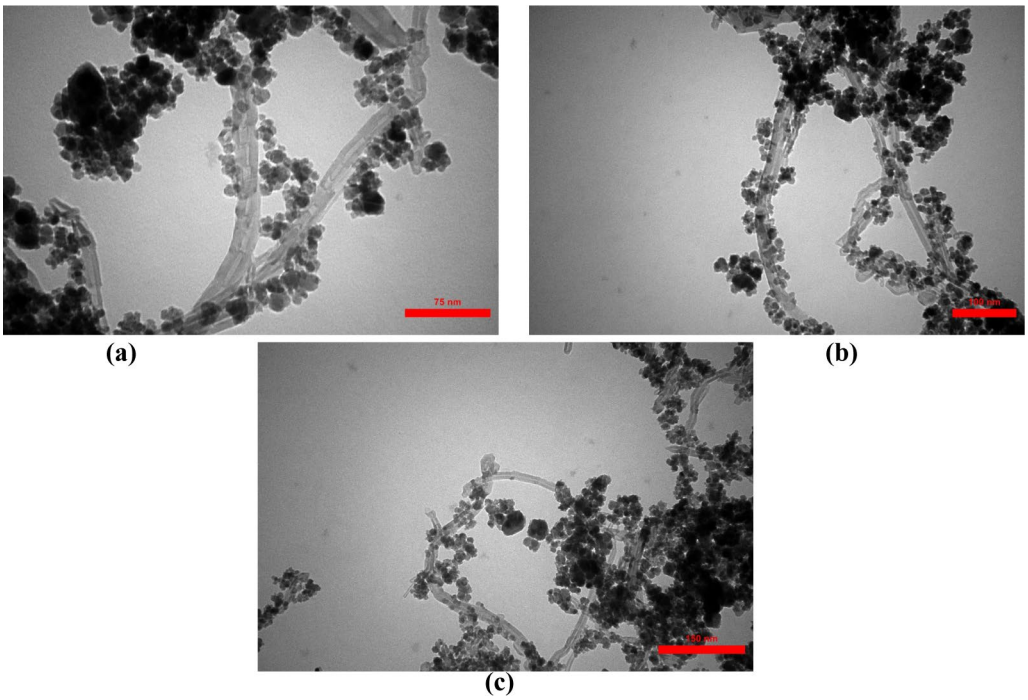

Fig. 2 TEM images of Fe_3O_4–MWCNT–ZIF67 at different magnifications (scale bars are: **a** 75 nm **b** 100 nm and **c** 150 nm)

regions in the images are due to the presence of Fe in Fe_3O_4 and Zn in ZIF-6, respectively, with higher atomic weight than carbon and oxygen elements in MWCNTs. As can be seen, the nanoparticles are aggregated to each other which cause to create thickness contrast in the images.

Figure 3 shows the EDS spectrum and elemental mapping analysis of Fe_3O_4–MWCNT-OH–ZIF67. The presence of Co and N in the spectrum of sample originates from the presence of ZIF-67. Furthermore, the characteristic peaks of Fe (K_α, K_β and L_β) arise from the Fe_3O_4 formation. The characteristic peaks of Fe, C, O, N and Co in spectrum confirm the formation of nanocomposite (Fig. 3A). The quantitative results of EDS analysis are included in the table (inset of Figure). Figure 3B shows the FE-SEM image of the selected area on the surface. The mapping analysis on the defined area shows the homogeneous distribution of the different elements.

Figure 4A shows the FTIR spectra of ZIF-67, Fe_3O_4–MWCNT-OH and Fe_3O_4–MWCNT–ZIF67 (before and after asorption). In the FTIR spectrum of Fe_3O_4–MWCNT, the characteristic peaks with wavenumbers of 1270, 1399 and 1715 cm^{-1} correspond to iron oxide nanoparticles and peak with wavenumber of 543 cm^{-1} is related to the stretching vibration of Fe–O bands [48]. The peaks at 1110 and 1649 cm^{-1} are attributed to multi-walled carbon nanotubes with hydroxyl functional groups of MWCNT-OH [40]. The peak at 2923 cm^{-1} is the asymmetric stretching adsorption of C–H bands [41]. The peak at 3414 cm^{-1} is due to the stretching vibrations of the O–H group.

In the FTIR spectrum of ZIF-67, the peak at 435 cm^{-1} is related to the stretching vibrations of the Co–N bands [40]. The peaks with wavenumbers in the range of 620 to 1419 cm^{-1} correspond to 2-methylimidazole [49]. The peak at 1170 cm^{-1} is related to the deformation vibrations within the plane of the C–H bands. The peaks at 1569 cm^{-1} and 1632 cm^{-1} are attributed to the vibrations of the imidazole rings [40]. The peak at 2922 cm^{-1} is related to the stretching of aliphatic C–H bands indicating the presence of 2-methylimidazole [50]. The characteristic peak of N–H bands, which is related to the combination of nitrogen atoms and metal ions, occurs at 3428 cm^{-1} [49]. The peak at 3682 cm^{-1} corresponds to the free O–H bands. The peak at 1715 cm^{-1} related to the C=O stretching is observed in the spectra of Fe_3O_4–MWCNT and ZIF-67. With formation of the nanocomposite, the intensities of peaks are decreased which confirms the formation of Fe_3O_4–MWCNT–ZIF67. In addition, as the nanocomposite was used in adsorption process of BUT (Fig. 4A), the intensity of peaks reduced substantially which means the interaction of BUT with Fe_3O_4–MWCNT–ZIF67.

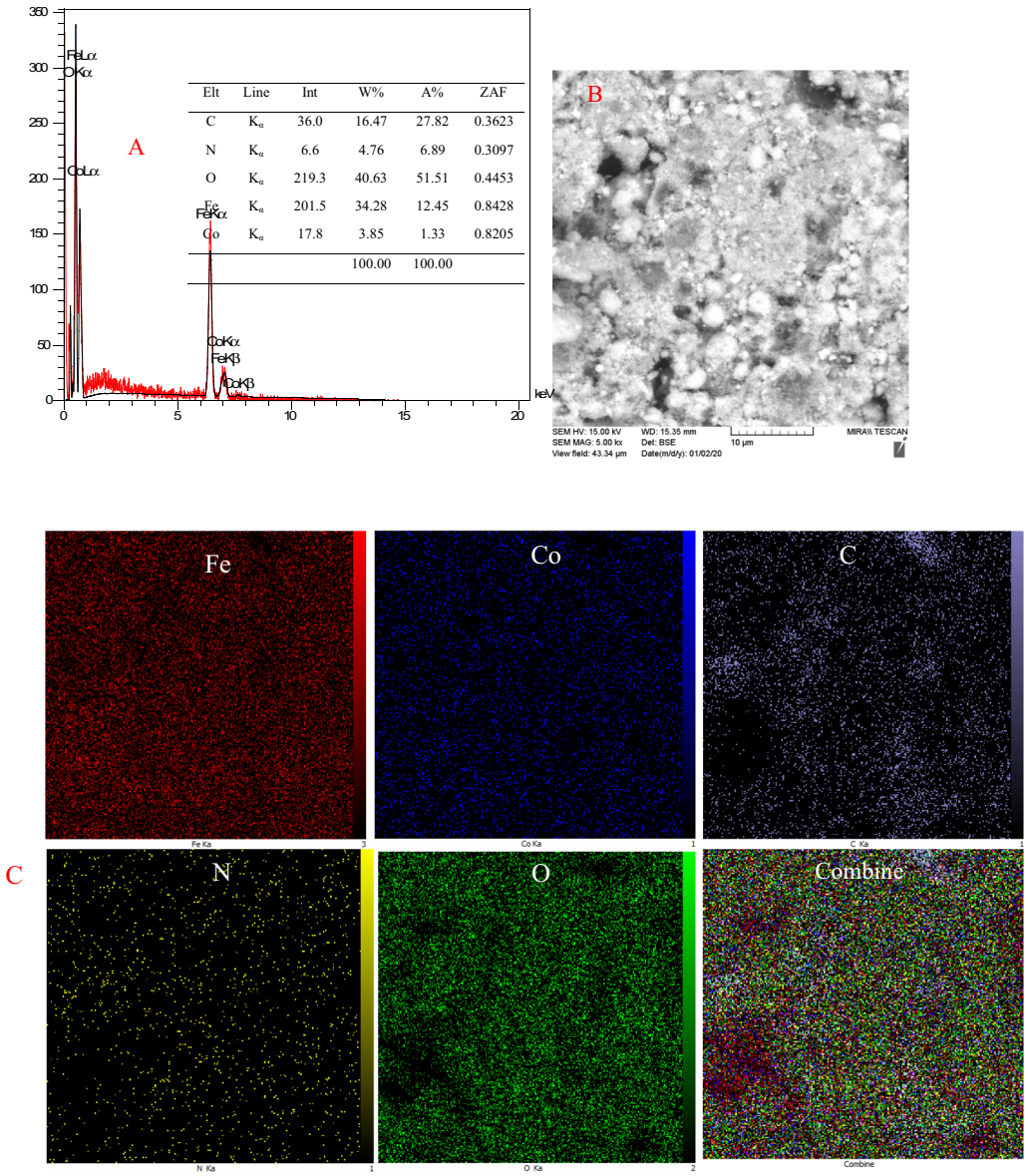

Fig. 3 **A** EDS analysis and **B** FE-SEM of selected area for Fe_3O_4–MWCNT–ZIF67 and **C** elemental mapping analysis for different elements

Figure 4B shows the XRD patterns of different samples. For ZIF-67, the characteristic peaks appeared in $2\theta = 10.6$, 12.7, 14.9, 16.8, 18.1, 19.7, 22.4, 25.3, 31.3 and 33.7°. For Fe_3O_4–MWCNT, the peaks at $2\theta = 30.7$, 35.98, 54.06, 57.43 and 63.11° are for Fe_3O_4 and the peaks at $2\theta = 26.96$ and 43.7° arise from the MWCNT. Due to the presence of MOF in Fe_3O_4–MWCNT–ZIF67, the peak intensities of nanocomposite were slightly decreased in comparison to Fe_3O_4–MWCNT [49].

Figure 5A shows N_2-adsorption and desorption isotherm of Fe_3O_4–MWCNT–ZIF67 composite. The isotherm is from type IV and has a hysteresis loop of type H3. BET surface area, specific surface area of pores, average pore diameter and total pore volume obtained from the analysis were 48.73 $m^2\ g^{-1}$, 53.175 $m^2\ g^{-1}$, 907.35 nm and 0.43662 $cm^3\ g^{-1}$, respectively. ZIF-67 has type I isotherms with microporous structure and provides high specific surface area of 1714 $m^2\ g^{-1}$ and total pore volumes of 0.631 $cm^3\ g^{-1}$. The comparison of the results shows that with mixing the MWCNTs, ZIF-67 and Fe_3O_4, the surface area of nanocomposite reduces and changes in physical and chemical properties have occurred.

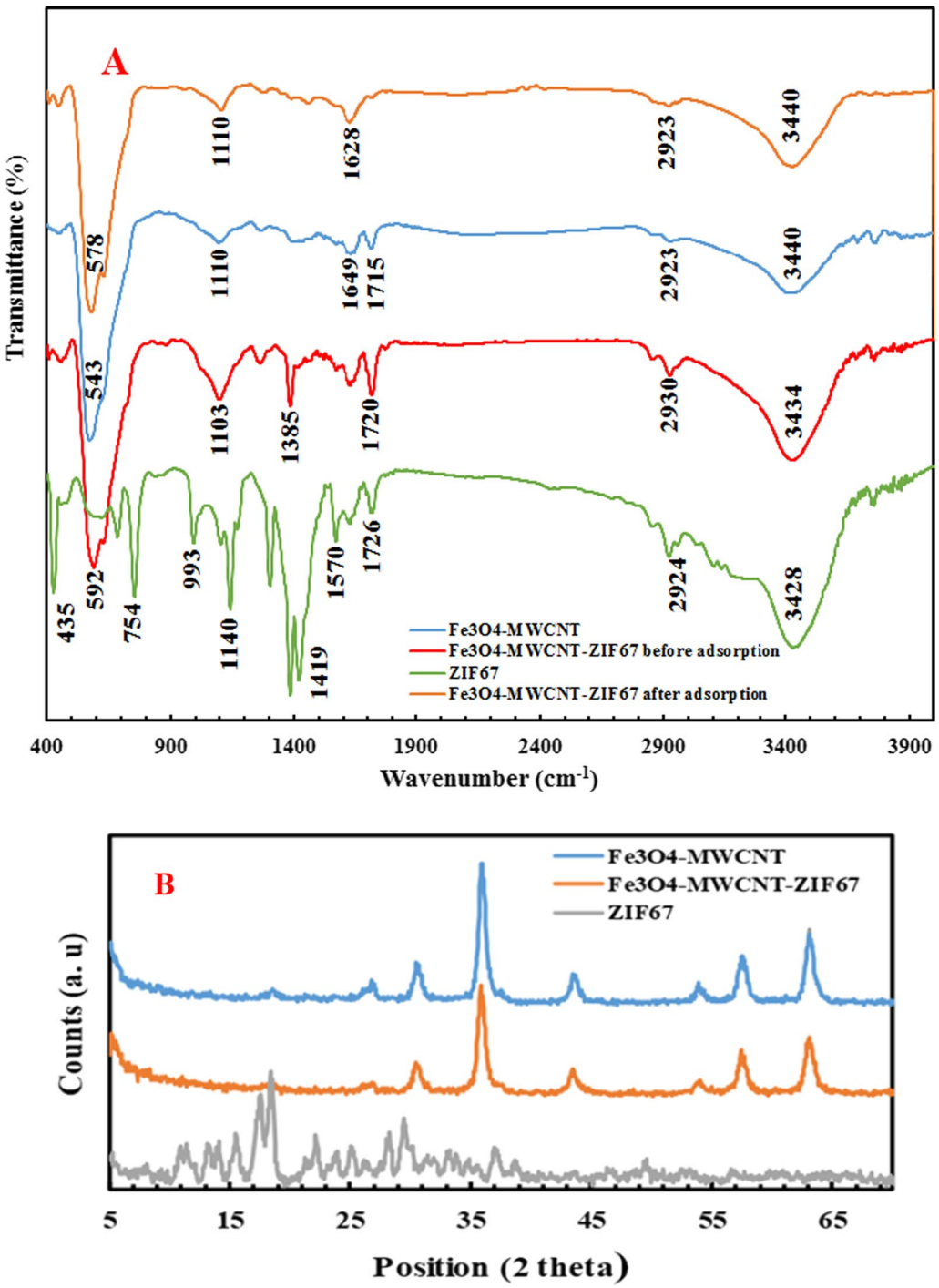

Fig. 4 **A** FTIR spectra and **B** XRD patterns of Fe_3O_4–MWCNT, Fe_3O_4–MWCNT–ZIF67, and ZIF-67

Figure 5B shows TGA curves for Fe_3O_4–MWCNT, Fe_3O_4–MWCNT–ZIF67 and ZIF-67. With increasing the temperature to 800 °C, a three-step weight loss is observed for ZIF-67 and reach to 90.91% of initial weight. The first stage of weight loss in the range of 25–275 °C is due to the loss of surface moisture in the sample. The second and third stage occurred in the range of 275–480 and 480–800 °C, respectively, which are attributed to the loss of trapped water and solvent and destroying the structure of MOF. The TGA curves

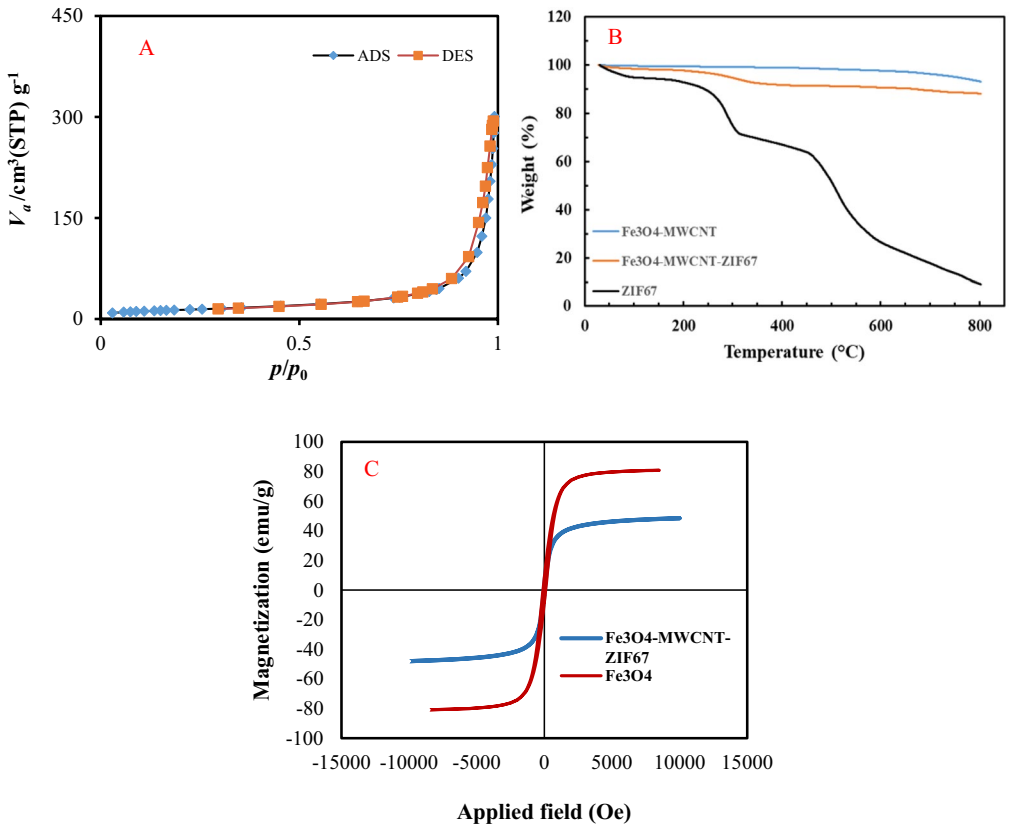

Fig. 5 **A** Adsorption–desorption isotherm of Fe_3O_4–MWCNT–OH/ZIF67, **B** TGA and **C** VSM curves of different samples

of Fe_3O_4–MWCNT and Fe_3O_4–MWCNT–ZIF67 show weight loss of 6.927 and 12%, respectively. MWCNT encounters with the weight loss due to removal of oxygen-containing groups. When Fe_3O_4 and MWCNT were added to ZIF-67 in nanocomposite, thermal stability was significantly increased and becomes stable [50].

The magnetic properties of the adsorbent were measured using VSM analysis at ambient temperature. Figure 5C shows the VSM curves for Fe_3O_4 and Fe_3O_4–MWCNT–ZIF67. No hysteresis loop is observed and the sample shows the superparamagnetic behavior which is due to the formation of Fe_3O_4. The presence of non-magnetic materials of MWCNT and ZIF-67 in nanocomposite reduced the magnetic property of iron oxide from 69.03 to 45.8 emu g^{-1} which is due to decreasing of non-magnetic saturation of the nanoparticles covered by the materials. Although the magnetic strength of the adsorbent is lower than that of Fe_3O_4 nanoparticles, the magnetic strength of the adsorbent is sufficient for easy separation from the aqueous solution by applying an external magnetic field.

Optimization

Among several possible models and according to the experimental results, a third-degree model can be fitted on the results. Equation 11 shows the resulting model in terms of the initial concentration (A), pH (C), adsorbent dose (B), temperature (E) and time (D) of solution with the following relation:

$$\begin{aligned} R\% = {} & 33.34 - 6.56A + 15.67B + 0.18C \\ & + 4.91D + 4.39E + 5.82AB + 8.5AC \\ & + 3.9AE + 4.57BE + 7.51A^2 - 8.85A^2E \end{aligned} \quad (11)$$

The parameter that has the great positive coefficient value in the equation indicates a greatly positive influence on the response. The mean squares, the degree of freedom, and the sum of squares were also obtained. Moreover, F and p-values were used to display when these terms are significant in the quadratic model. Data reported in Table 2 exhibit that all coefficients are significant. The significance of the quadratic model with consideration of Table 1 is presented in Table 3.

The accuracy of the designed equations is expressed by the convergence coefficient R^2. The R^2 and R^2_{adj} values of

Table 3 Results of model analysis of variance

Source	Sum of squares	Degrees of freedom	Average total squares	*F* value	*P* value
Model	12,056.52	11	1096.05	20.96	< 0.0001
A (concentration)	1031.69	1	1031.69	19.73	0.0002
B (dosage)	589,978	1	5859.78	112.62	< 0.0001
C (pH)	0.82	1	0.82	0.016	0.0994
D (time)	579.15	1	579.15	11.07	0.0029
E (temp)	154.18	1	154.18	2.95	0.0994
Residual	1202.81	23	52.30		

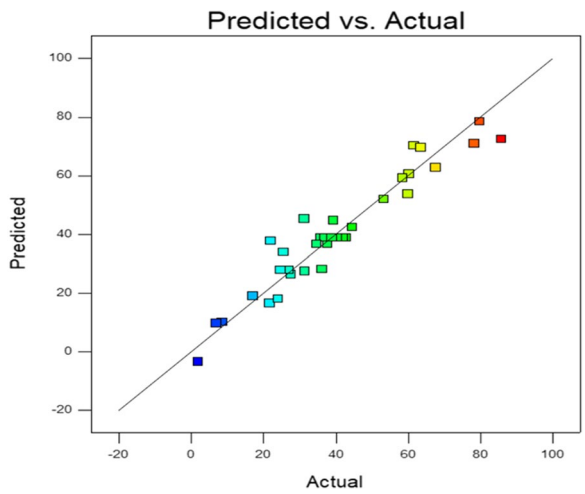

Fig. 6 The predicted data versus actual data obtained by experimental data removal efficiency of BUT

the model are 0.91 and 0.86, respectively, which is in good agreement with the experimental values. Figure 6 shows the correspondence between experimental data and the predicted response by the RSM optimization approach. Data closer to the line represent small difference between the experimental and the predicted responses. Therefore, a good optimal point can be obtained from the designed experiment.

Analysis of three-dimensional response surface curves

To better understand each response surface, three-dimensional curves of effective parameters in the presence of BUT removal percentage were plotted and analyzed (Fig. 7). In these curves, a pair of parameters is displayed while other factors are kept constant. Figure 7a shows the response surface curve of the removal percentage with the initial BUT concentration and the adsorbent dosage. According to the proposed model (i.e., Eq. 11), the initial concentration of BUT has a negative effect on the adsorption percentage. The reason for decreasing the removal percentage is that with increasing the initial concentration of BUT from 5.75 to 13.25 ppm, the mole of contaminant increases, but there is a given amount of adsorbent in the solution, in other words, the active adsorption sites are constant.

The adsorbent dose has a positive effect on the removal percentage because the adsorbent active sites on the surface are higher than the adsorbate molecule. However, with increasing the adsorbent dose to values higher than 0.07 g in 50 mL solution, the active sites become saturated in the surface, therefore, the removal percentage decreases. However, considering the interaction of two parameters on the removal percentage, it showed a positive effect on the removal process of BUT. An increase in the percentage of BUT removal by decreasing the initial concentration from 13.25 to 5.75 ppm and increasing the adsorbent dosage from 0.03 to 0.07g are also observed.

Figure 7b shows the response surface curve of the removal percentage with the initial BUT concentration and pH. According to the proposed model (i.e., Eq. 11), the initial concentration of BUT and pH have negative effect on BUT removal percentage, so that with increasing pH from 4.5 to 7.5, the removal percentage decreases. In the natural and alkaline pH range, the percentage of BUT removal is negligible because BUT has anionic form due to the presence of carboxylic and phenolic groups. However, the adsorbent surface is positively charged at low (acidic) pH range 4.5 and converts to the cationic form, thus establishing a strong electrostatic bond between the adsorption surface and BUT, causes further removal of BUT. However, considering the interaction of both parameters, the removal percentage had a positive effect.

Figure 7c shows the response surface curve of percentage of BUT removal with the initial BUT concentration and temperature. According to the proposed model (i.e., Eq. 11), the initial concentration of BUT has a negative effect and the temperature has a positive effect, so that if the process is endothermic, the

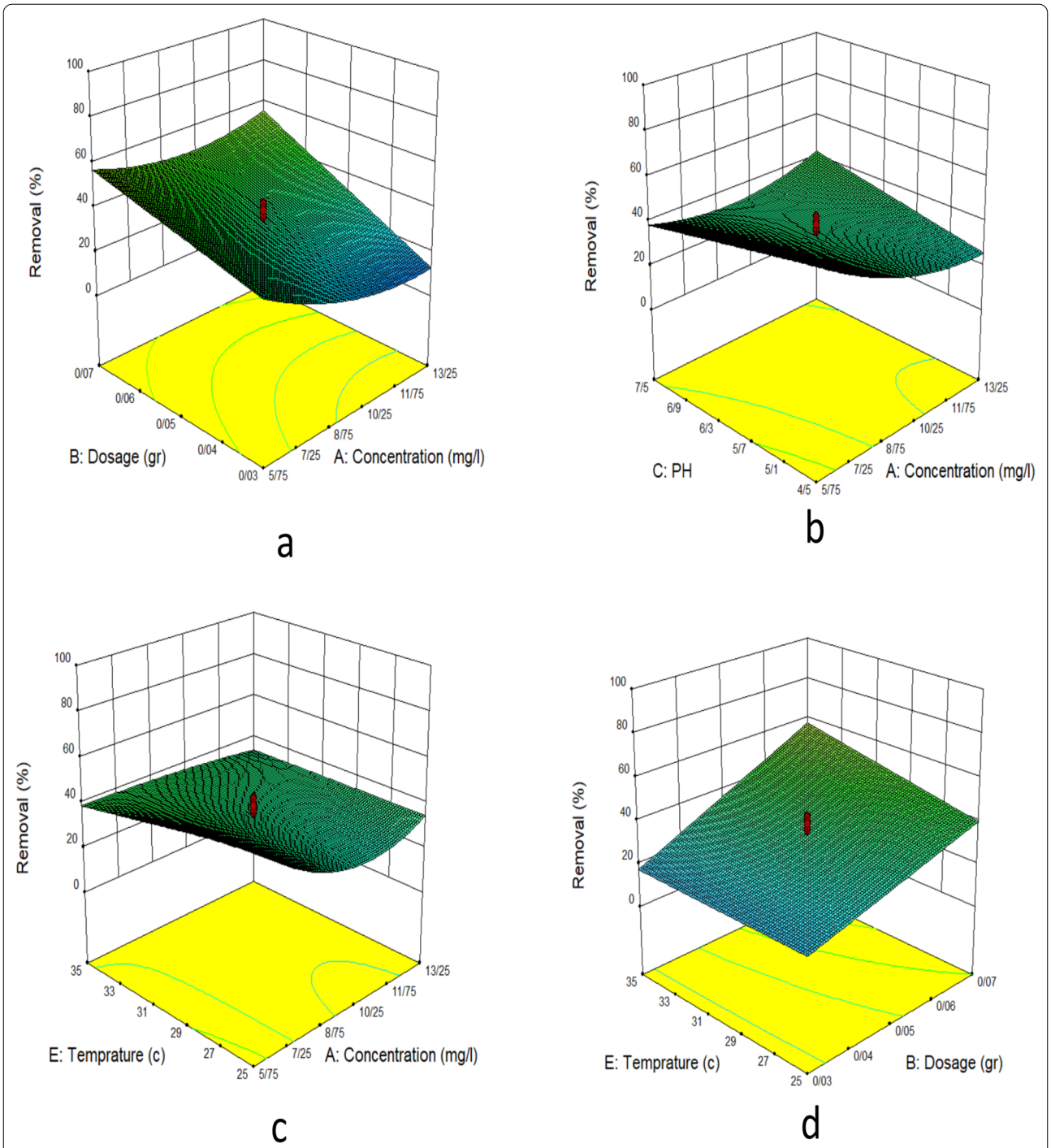

Fig. 7 Effect of factors on BUT Removal (%) RSM plots

kinetic energy of the pollutant increases with increasing temperature from 25 to 35 °C and the probability of their collision with the adsorbent surface increases. However, considering the interaction of the two parameters, it has a positive effect on the removal percentage trend.

Figure 7d shows the response surface curve of percentage of BUT removal with adsorbent dosage and temperature. An increase in percentage of BUT removal is also observed by increasing the adsorbent dosage from 0.03 to 0.07 g and the temperature from 25 to 35 °C. According to the model, both of them have positive effects.

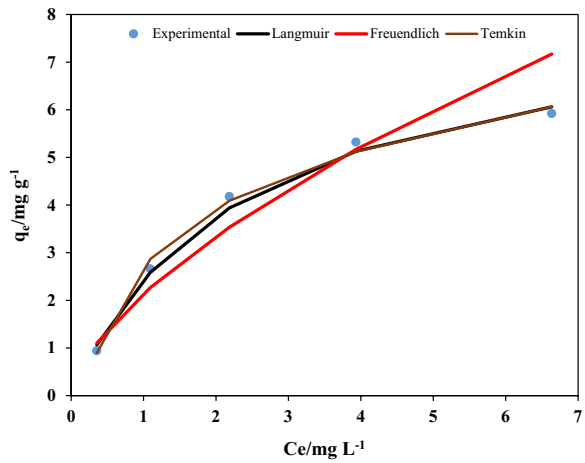

Fig. 8 Equilibrium adsorption data (V = 40 mL, dosage = 0.07gr, pH = 4.5 and temp = 35 °C)

Table 4 Parameters obtained from fitting equilibrium data with different isotherms

Model	Parameters	Amounts
Langmuir	q_{max} (mg g^{-1})	8.2440
	K_L (L mg^{-1})	0.4188
	R^2	0.988
Freundlich	n	1.5698
	K_F ($mg^{1-(1/n)}$ $L^{1/n}$ g^{-1})	2.1492
	R^2	0.942
Temkin	B_T (J mol^{-1})	1.7659
	K_T (L g^{-1})	4.6427
	R^2	0.993

Figure 8 represents the adsorption isotherm of BUT on Fe_3O_4–MWCNT–ZIF-6. Equilibrium parameters related to above isotherms are presented in Table 4. The results show that the Temkin isotherm is in good agreement with equilibrium data. The highest value of R^2 for the Temkin isotherm (R^2 = 0.993) in comparison to Langmuir (R^2 = 0.988) and Freundlich (R^2 = 0.942) isotherms

Table 5 Parameters of kinetic models

C_0 (mg L^{-1})	$q_{e,exp}$ (mg g^{-1})	Pseudo-first order		Pseudo-second order	
		k_1	R^2	k_2	R^2
2	0.9404	0.0110	0.9523	0.1466	0.9922
5.75	2.6605	0.0110	0.9523	0.0506	0.9919
9.5	4.1791	0.0110	0.9523	0.0299	0.99
13.25	5.3234	0.0110	0.9523	0.0198	0.9889
17	5.9219	0.0071	0.9821	0.0802	0.9827

proved that the interactions between the Fe_3O_4–MWCNT–ZIF-6 and the BUT are considered.

In addition, from Tables 5 and 6, different models are fitted with kinetic data. As can be seen, the pseudo-first-order equation, Elovich and intra-particle diffusion models do not fit well, but the pseudo-second-order equation can be properly fitted.

The thermodynamic quantities are calculated from the Van't Hoff equation plot (Fig. 9) and summarized in Table 7. Based on the results, the negative values of $\Delta G°$ indicate the spontaneous as well as the physicality (range of 0 to 20 kJ mol^{-1}) of the adsorption process. The positive value of $\Delta H°$ is a representative of the endothermic process. The positive value of $\Delta S°$ also demonstrates the increase of irregularities in the interface of liquid–solid during the adsorption, which exhibits the enhancement of the performance for BUT adsorption.

Conclusions

In this research, the ability of Fe_3O_4–MWCNT–ZIF67 adsorbent was studied for BUT removal from the aqueous solution. RSM and CCD analyses were used to optimize the important adsorption parameters (i.e., adsorbent dosage, initial concentration, pH, contact time and temperature). The optimum adsorption conditions predicted by RSM were pH = 4.5, initial concentration = 5.75 ppm, dosage = 0.07 g and contact time = 95 min. The kinetic data are better fitted to the pseudo-second-order kinetic model.

Table 6 Parameters of kinetic models

C_0 (mg L^{-1})	$q_{e,exp}$ (mg g^{-1})	Elovich model			Intra-particle diffusion model		
		β	α	R^2	K	C	R^2
2	0.9404	0.852	18.572	12.722	0.972	0.5258	0.0272
5.75	2.6605	0.8281	50.151	4.504	0.9225	1.481	0.0765
9.5	4.1791	0.8521	40.64	2.678	0.972	2.21	0.1293
13.25	5.3234	0.8521	21.545	1.921	0.972	2.5771	0.181
17	5.9219	0.8377	3678.059	2.323	0.65	4.5922	0.123

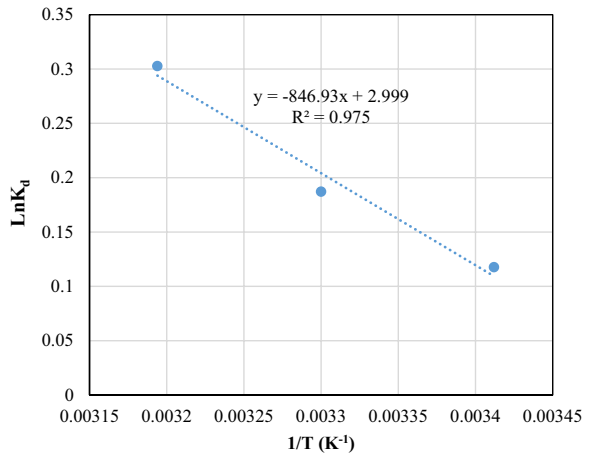

Fig. 9 Plot of Van't Hoff equation in the range of 293–313 K (C_0: 5.75 ppm, adsorbent dosage: 0.07 g, pH 4.5, and contact time: 95 min)

Table 7 Thermodynamic parameters for the adsorption of BUT

Temp (K)	$\Delta G°$ (kJ mol^{-1})	$\Delta H°$ (kJ mol^{-1})	$\Delta S°$ (J mol^{-1} K^{-1})
293	− 18.558	7.041	24.9336
303	− 20.3619		
313	− 22.2357		

Comparison between the regression coefficients of different isotherm models indicates that Temkin isotherm is in a good agreement with equilibrium data. It was concluded from the thermodynamic investigations that the removal of BTU by the adsorbent is spontaneous and endothermic.

Acknowledgements
The authors are grateful to Iran National Science Foundation (INSF) Grant No. 99008622, for their kind financial support on the research.

Author contributions
AAA: writing—original draft, supervision. SG: conceptualization, review and editing. AA: writing—original draft, doing experimental. All authors read and approved the final manuscript.

Funding
Not applicable.

Availability of data and materials
All data generated or analyzed during this study are included in this published article.

Declarations

Ethics approval consent to participate
Not applicable.

Consent for publication
Not applicable.

Competing interests
The authors declare no competing interests.

Author details
[1]Department of Chemical Engineering, Technology and Engineering of Faculty, University of Mazandaran, Babolsar, Iran. [2]Faculty of Chemistry, University of Mazandaran, Babolsar, Iran.

Received: 25 January 2022 Accepted: 1 May 2022
Published online: 03 June 2022

References

1. Akbarlou Z, Alipour V, Heidari M, Dindarloo K (2017) Adsorption of diazinon from aqueous solutions onto an activated carbon sample produced in Iran. Environ Health Eng Manag 4(2):93–99
2. Fulekar MH (2014) Rhizosphere bioremediation of pesticides by microbial consortium and potential microorganism. Curr Microbiol Appl Sci 3(7):235–248
3. Dong M, Ma Y, Zhao E, Qian C (2009) Using multiwalled carbon nanotubes as solid phase extraction adsorbents for determination of chloroacetanilide herbicides in water. Microchim Acta 165(1–2):123–128
4. Mahadi MA, Dadari SA, Mahmud M, Babaji BA, Mani H (2007) Effect of some rice based herbicides on yield and yield components of maize. Crop Prot 26(11):1601–1605
5. Chen J, Cao S, Xi C, Chen Y, Li X, Zhang L, Wang G, Chen Y, Chen Z (2018) A novel magnetic β-cyclodextrin modified graphene oxide adsorbent with high recognition capability for 5 plant growth regulators. Food Chem 239:911–919
6. Guan W, Long Z, Liu J, Hua Y, Ma Y, Zhang H (2015) Unique graphitic carbon nitride nanovessels as recyclable adsorbent for solid phase extraction of benzoylurea pesticides in juices samples. Food Anal Methods 8(9):2202–2210
7. Zhang M, Yang J, Geng X, Li Y, Zha Z, Cui S, Yang J (2019) Magnetic adsorbent based on mesoporous silica nanoparticles for magnetic solid phase extraction of pyrethroid pesticides in water samples. J Chromatogr A 1598:20–29
8. He L, Cui W, Wang Y, Zhao W, Xiang G, Jiang X, Zhang S (2017) Polymeric ionic liquid based on magnetic materials fabricated through layer-by-layer assembly as adsorbents for extraction of pesticides. J Chromatogr A 1522:9–15
9. Wang X, Meng X, Wu Q, Wang C, Wang Z (2019) Solid phase extraction of carbamate pesticides with porous organic polymer as adsorbent followed by high performance liquid chromatography-diode array detection. J Chromatogr A 1600:9–16
10. Liu G, Li L, Huang X, Zheng S, Xu X, Liu Z, Zhang Y, Wang J, Lin H, Xu D (2018) Adsorption and removal of organophosphorus pesticides from environmental water and soil samples by using magnetic multi-walled carbon nanotubes@ organic framework ZIF-8. J Mater Sci 53(15):10772–10783
11. Hayati B, Maleki A, Najafi F, Daraei H, Gharibi F, McKay G (2017) Super high removal capacities of heavy metals (Pb2+ and Cu2+) using CNT dendrimer. J Hazard Mater 15(336):146–157
12. Carrales-Alvarado DH, Leyva-Ramos R, Rodríguez-Ramos I, Mendoza-Mendoza E, Moral-Rodríguez AE (2020) Adsorption capacity of different types of carbon nanotubes towards metronidazole and dimetridazole antibiotics from aqueous solutions: effect of morphology and surface chemistry. Environ Sci Pollut Res 27(14):17123–17137
13. Maleki A, Hamesadeghi U, Daraei H, Hayati B, Najafi F, McKay G, Rezaee R (2017) Amine functionalized multi-walled carbon nanotubes: single and binary systems for high capacity dye removal. Chem Eng J 1(313):826–835
14. Shimizu Y, Ateia M, Yoshimura CJC (2018) Natural organic matter undergoes different molecular sieving by adsorption on activated carbon and carbon nanotubes. Chemosphere 203:345–352
15. Rashed MN (2013) Adsorption technique for the removal of organic pollutants from water and wastewater, in organic pollutants-monitoring, risk and treatment. IntechOpen, London
16. Li S, Li Z, Ke B, He Z, Cui Y, Pan Z, Li D, Huang S, Lai C, Su J (2019) Magnetic multi-walled carbon nanotubes modified with polyaluminium chloride for removal of humic acid from aqueous solution. J Mol Liq 1(279):241–250

17. Abazari R, Mahjoub AR, Shariati J (2019) Synthesis of a nanostructured pillar MOF with high adsorption capacity towards antibiotics pollutants from aqueous solution. J Hazard Mater 366:439–451
18. He Y, Chen F, Li B, Qian G, Zhou W, Chen B (2018) Porous metal–organic frameworks for fuel storage. Coord Chem Rev 15(373):167–198
19. Wu H, Thibault CG, Wang H, Cychosz KA, Thommes M, Li J (2016) Effect of temperature on hydrogen and carbon dioxide adsorption hysteresis in an ultramicroporous MOF. Microporous Mesoporous Mater 1(219):186–189
20. Dong D, Yan C, Huang J, Lu N, Wu P, Wang J, Zhang Z (2019) An electron-donating strategy to guide the construction of MOF photocatalysts toward co-catalyst-free highly efficient photocatalytic H 2 evolution. J Mater Chem A 7(42):24180–24185
21. Koo WT, Jang JS, Kim IDJC (2019) Metal-organic frameworks for chemiresistive sensors. Chem 5(8):1938–1963
22. Hartlieb KJ, Holcroft JM, Moghadam PZ, Vermeulen NA, Algaradah MM, Nassar MS, Botros YY, Snurr RQ, Stoddart JF (2016) CD-MOF: a versatile separation medium. J Am Chem Soc 138(7):2292–2301
23. Li X, Liu Y, Wang J, Gascon J, Li J, Van der Bruggen B (2017) Metal–organic frameworks based membranes for liquid separation. Chem Soc Rev 46(23):7124–7144
24. Zhao SN, Song XZ, Song SY, Zhang HJ (2017) Highly efficient heterogeneous catalytic materials derived from metal-organic framework supports/precursors. Coord Chem Rev 15(337):80–96
25. Mu L, Liu B, Liu H, Yang Y, Sun C, Chen G (2012) A novel method to improve the gas storage capacity of ZIF-8. J Mater Chem 22(24):12246–12252
26. Huang A, Chen Y, Wang N, Hu Z, Jiang J, Caro J (2012) A highly permeable and selective zeolitic imidazolate framework ZIF-95 membrane for H 2/CO 2 separation. Chem Commun 48(89):10981–10983
27. Yang J, Zhang F, Lu H, Hong X, Jiang H, Wu Y, Li Y (2015) Hollow Zn/Co ZIF particles derived from core–shell ZIF-67@ ZIF-8 as selective catalyst for the semi-hydrogenation of acetylene. Angew Chem 127(37):11039–11043
28. Zhou L, Li N, Owens G, Chen Z (2019) Simultaneous removal of mixed contaminants, copper and norfloxacin, from aqueous solution by ZIF-8. Chem Eng J 15(362):628–637
29. Meng W, Wen Y, Dai L, He Z, Wang L (2018) A novel electrochemical sensor for glucose detection based on Ag@ ZIF-67 nanocomposite. Sens Actuators, B Chem 1(260):852–860
30. Chen L, Wang J, Shen X, Li X, Duan C (2019) ZIF-67@ Co-LDH yolk–shell spheres with micro-/meso-porous structures as vehicles for drug delivery. Inorg Chem Front 6(11):3140–3145
31. Dhaka S, Kumar R, Deep A, Kurade MB, Ji SW, Jeon BH (2019) Metal–organic frameworks (MOFs) for the removal of emerging contaminants from aquatic environments. Coord Chem Rev 1(380):330–352
32. Li WK, Zhang HX, Shi Y-P (2017) Selective adsorption of aromatic acids by a nanocomposite based on magnetic carboxylic multi-walled carbon nanotubes and novel metal-organic frameworks. Appl Surf Sci 416:672–680
33. Yang Q, Ren S, Zhao Q, Lu R, Hang C, Chen Z, Zheng H (2018) Selective separation of methyl orange from water using magnetic ZIF-67 composites. Chem Eng J 333:49–57
34. Liang C, Zhang X, Feng P, Chai H, Huang Y (2018) ZIF-67 derived hollow cobalt sulfide as superior adsorbent for effective adsorption removal of ciprofloxacin antibiotics. Chem Eng J 15(344):95–104
35. Sun X, Xu W, Zhang X, Lei T, Lee SY, Wu Q (2021) ZIF-67@ cellulose nanofiber hybrid membrane with controlled porosity for use as Li-ion battery separator. J Energy Chem 1(52):170–180
36. Abdelkader-Fernández VK, Fernandes DM, Balula SS, Cunha-Silva L, Freire C (2020) Advanced framework-modified POM@ ZIF-67 nanocomposites as enhanced oxygen evolution reaction electrocatalysts. J Mater Chem A 8(27):13509–13521
37. Shang H, Xu H, Jin L, Chen C, Song T, Wang C, Du Y (2019) Electrochemical-photoelectrochemical dual-mode sensing platform based on advanced Cu9S8/polypyrrole/ZIF-67 heterojunction nanohybrid for the robust and selective detection of hydrogen sulfide. Sens Actuators, B Chem 12(301):127060
38. Nozhat S, Hassani AH, Panahi HA, Moniri E, Monavari M (2018) Elimination and absorption of butachlor from water aqueous containing herbicide by modified magnetic graphene oxide. Desalin Water Treat 1(136):273–281
39. Liu X, Wang C, Wu Q, Wang Z (2015) Metal-organic framework-templated synthesis of magnetic nanoporous carbon as an efficient absorbent for enrichment of phenylurea herbicides. Anal Chim Acta 22(870):67–74
40. Wei X, Wang Y, Chen J, Xu P, Zhou Y (2018) Preparation of ionic liquid modified magnetic metal-organic frameworks composites for the solid-phase extraction of α–chymotrypsin. Talanta 15(182):484–491
41. Feng X, Lin S, Li M, Bo X, Guo L (2017) Comparative study of carbon fiber structure on the electrocatalytic performance of ZIF-67. Anal Chim Acta 1(984):96–106
42. Moosa AA, Ridha AM, Kadim NA (2016) use of biopolymer adsorbent in the removal of phenol from aqueous solution. Am J Mater Sci 6(4):94–104
43. Lagergren S (1898) About the theory of so-called adsorption of soluble substances. Handlingar 24:1–39
44. Ho YS, Mckay G (1998) A comparison of chemisorption kinetic models applied to pollutant removal on various sorbents. Process Saf Environ Prot 76:332–340
45. Sengil A, Ozacar M (2005) A kinetic study of metal complex dye sorption onto pine sawdust. Process Biochem 40:565–572
46. Valderrama C, Gamisans X, Heras X, De Farr A, Cortina JL (2008) Sorption kinetics of polycyclic aromatic hydrocarbons removal using granular activated carbon: intraparticle diffusion coefficients. J Hazard Mater 157:386–396
47. Lima EC, Hosseini-Bandegharaei A, Moreno-Piraj´an JC, Anastopoulos I. A critical review of the estimation of the thermodynamic parameters on adsorption equilibria. Wrong use of equilibrium constant in the Van't Hoof equation for calculation of thermodynamic parameters of adsorption. J Mol Liquids. 2019; 273: 425–434
48. Huang X, Liu G, Xu D, Xu X, Li L, Zheng S, Lin H, Gao H (2018) Novel zeolitic imidazolate frameworks based on magnetic multiwalled carbon nanotubes for magnetic solid-phase extraction of organochlorine pesticides from agricultural irrigation water samples. Appl Sci 8(6):959
49. Li WK, Chen J, Zhang HX, Shi YP (2017) Selective determination of aromatic acids by new magnetic hydroxylated MWCNTs and MOFs based composite. Talanta 1(168):136–145
50. Lin KYA, Lee WD (2016) Self-assembled magnetic graphene supported ZIF-67 as a recoverable and efficient adsorbent for benzotriazole. Chem Eng J 284:1017–1027

Publisher's Note